



Tuning Ideal Tensile Strengths and Intrinsic Ductility of bcc Refractory Alloys

Liang Qi and D. C. Chrzan*

Department of Materials Science and Engineering, University of California, Berkeley, California 94720, USA

(Received 4 September 2013; revised manuscript received 21 January 2014; published 19 March 2014)

An important theoretical ductility criterion for group V and VI metal-based refractory alloys in body-centered cubic (bcc) lattices is the mechanical failure mode of their perfect crystals under tension along the weakest direction [100]. Pure Mo and W fail by cleavage and are deemed intrinsically brittle. However, first-principles calculations show that alloying with group IV or V transition metals can transform these materials into ones that display intrinsically ductile behavior, failing in shear under [100] tension. Remarkably, this transition can be understood as an electron filling effect with the intrinsically ductile response the manifestation of a Jahn-Teller distortion.

DOI: 10.1103/PhysRevLett.112.115503

PACS numbers: 62.20.fk, 62.20.mj

Refractory alloys based on group VI metals, molybdenum (Mo) and tungsten (W), are attractive for many important high-temperature applications, including critical components in fusion reactors and turbine engines [1–3]. However, they display a ductile-brittle transition as temperature drops, and their transition temperatures can be close to or even higher than room temperature depending on material microstructures and strain rates [4,5]. Thus, the lack of ductility at room temperature and even moderately high temperature is a critical bottleneck that limits large-scale industrial applications of Mo and W alloys [1,2].

There are two aspects of a material's ductility that can be addressed during alloy design. Most commonly, researchers focus on modifying the so-called extrinsic features of the alloy (e.g., grain size, precipitate distribution, etc.) to passivate and blunt cracks before they propagate and lead to failure of the macroscopic part [2,6]. One can also focus on a second aspect of the alloy behavior, the intrinsic ductility of its perfect crystal. From the stress perspective, dislocation nucleation requires that the local shear stress on the slip plane should be near the corresponding ideal shear strength, while crack initiation requires that the local tensile stress on the direction perpendicular to the cleavage plane should be larger than the ideal tensile strength [7]. However, even under the loading direction perpendicular to the cleavage plane, some materials in perfect crystalline structures reach ideal shear strength along other orientations first so that they fail by shear deformation [8]. Under this circumstance of "shear instability," dislocation nucleation will be activated before crack formation, and the materials will be intrinsically ductile.

First-principles calculations have been used to investigate ideal tensile or shear strengths and the related shear instabilities [9–15]. For bcc metals, $\langle 100 \rangle$ is the weakest direction under tension [16,17]. It was found that under $\langle 100 \rangle$ tension group-V transition metals V and Nb fail by shear deformation, where the tetragonal symmetry of the strained bcc crystal is broken by the shear instability indicated in

Figs. 1(a) and 1(b) before the ideal tensile strength is reached [11,14]. These materials are, thus, intrinsically ductile. On the other hand, the shear instability occurs after the ideal tensile strength is reached for both Mo and W, so they are intrinsically brittle [10,11]. One expects that starting with an intrinsically ductile material will lead to a more ductile final product, and, indeed, in industrial applications group V—based refractory alloys show better ductility and toughness than group VI—based refractory alloys [1].

In this study, we apply first-principles calculations to show that Mo and W based alloys can become intrinsically ductile if their average valence electron numbers are decreased by alloying. Moreover, detailed analyses of the electronic structures show that the shear instability necessary for intrinsic ductility is simply a Jahn-Teller distortion that lowers the total energy of the alloy by splitting the degenerate energy levels of symmetry-related and partially occupied orbitals near the Fermi level [Figs. 1(c) and 1(d)] [18,19].

For illustrative purpose, we use two types of supercells to describe the change of the original bcc structure under tension, as shown in Fig. 1(a). One is the original cubic supercell with two atoms; the other is a tetragonal supercell with four atoms. The [100] axis \mathbf{a}_1 in the cubic supercell is the same as the [100] axis \mathbf{b}_1 in the tetragonal supercell, while \mathbf{b}_2 and \mathbf{b}_3 in the tetragonal supercell are $[011]_{\text{bcc}}$ and $[0\bar{1}1]_{\text{bcc}}$, respectively. After applying a fixed tensile strain ε_{11} along the [100] direction, we relax the supercell along the other directions so that all the stress tensor components $\sigma_{ij} < 0.05$ GPa, except σ_{11} . Here, σ_{11} is the true stress and ε_{11} is the engineering strain $\Delta|\mathbf{a}_1|/|\mathbf{a}_1|(\varepsilon_{11} = 0)$. If this relaxed configuration maintains tetragonal symmetry, we say that the deformation proceeds on the tetragonal path (TP). Increasing the strain, however, can lead to a configuration displaying a shear instability [Fig. 1(b)]. Here, the tetragonal cell is transformed to an orthorhombic structure ($|\mathbf{b}_2| \neq |\mathbf{b}_3|$). This deformation path is referred to as the orthorhombic path (OP).

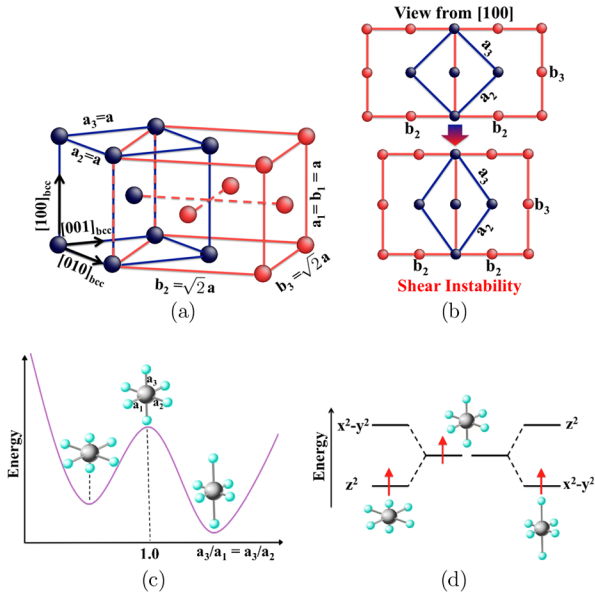


FIG. 1 (color online). (a) Body-centered cubic structures described by two-atom cubic supercell (in blue frame with dark blue atoms) and four-atom tetragonal supercell (in red frame). (b) Shear deformation occurs ($|\mathbf{b}_2| \neq |\mathbf{b}_3|$) when ε_{11} is above a critical value, then the original $[010]_{\text{bcc}}(\mathbf{a}_2)$ and $[001]_{\text{bcc}}(\mathbf{a}_3)$ are not perpendicular to each other. (c), (d) Jahn-Teller energetics for a molecule with octahedral symmetry. The e_g level is shown, with an electron occupation corresponding to d^1 (replications of the illustrative figures in Ref. [19]).

We employed density functional theory using the Vienna *Ab initio* Simulation Package (VASP) [20] and QUANTUM ESPRESSO (QE) [21] assuming non-spin-polarized conditions. VASP was used for pure metals and alloys in the B2 structure, where the body-center site in the bcc lattice is replaced by another transition metal atom (correspondingly, two face-center sites in the tetragonal supercell are replaced by alloying atoms); QE was used for pure metals and alloys in the virtual crystal approximation (VCA) scheme [22], where pseudopotentials of two elements are averaged into a composite pseudopotential for the study of properties of random solid solutions. In VASP, pseudopotentials generated by the projector augmented wave method within the generalized gradient approximation were applied [23,24]. In QE, norm-conserving pseudopotentials were generated by the Martins-Troullier method in the Perdew-Burke-Ernzerhof (PBE) exchange-correlation functional [25,26]. Norm-conserving PBE pseudopotentials for VCA calculations were generated by using the FHI98PP program with intermediate nuclear charges [27]. For VASP, Brillouin zone integrations were performed on a grid of $21 \times 21 \times 21$ points for the two-atom cubic supercell and $23 \times 17 \times 17$ points for the four-atom tetragonal supercell, respectively, using a kinetic cutoff energy of 326 eV and a first-order Methfessel-Paxton smearing of 0.4 eV. For QE, the same calculations were performed in the primitive cell of only one atom for both the TP and OP with a kinetic energy cutoff of

612 eV. The strain ε_{11} was added with a step size of 0.02 from 0.00 to 0.30 for both the TP and OP. The stress-strain behaviors and failure modes from both codes agree with each other, indicating that the deformation mechanisms of these perfect crystal structures do not depend on the detailed calculation methods.

The results of [100] tension along both the TP and OP for different bcc metals are shown in Fig. 2 and Fig. S1 in the Supplemental Material [28]. The results for pure group V and group VI metals agree with previous studies [10,11,14]. When ε_{11} is small, the stress-strain relations along the two paths are identical. Along the TP, σ_{11} reaches the value of the ideal tensile strength σ_{11}^{IT} , which is defined as the value of σ_{11} corresponding to the smallest ε_{11} where $(d\sigma_{11}/d\varepsilon_{11}) \leq 0$, and then decreases smoothly; on the other hand, along the OP above a certain critical strain the shear instability occurs. At these points, as shown in Fig. 2(d), a bifurcation appears along the curves that describe the variation of \mathbf{b}_2 and \mathbf{b}_3 . For pure metals in group V the bifurcation occurs before the saddle point along the TP (especially for V and Nb, the shear instability occurs even when $\varepsilon_{11} \sim 0.02$), so σ_{11}^{IT} along the OP is smaller than its counterpart along the TP. Thus, these materials would fail in shear and they are intrinsically ductile. On the other hand, for the pure group VI metals Mo and W, the shear instability and the corresponding stress drop occurs only after σ_{11} reaches σ_{11}^{IT} along the TP, so the materials would fail by cleavage and are intrinsically brittle.

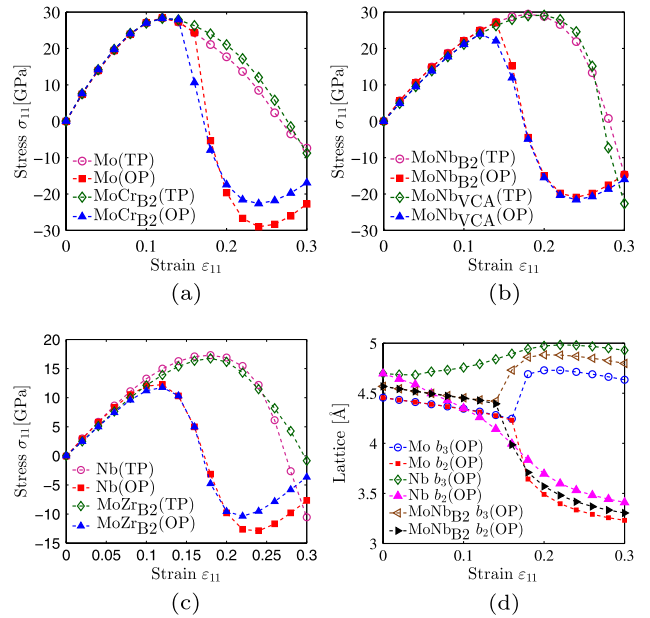


FIG. 2 (color online). (a)–(c) Stress-strain curves for different transition metal and alloys. (a) Pure Mo and MoCr in B2 structure ($\text{MoCr}_{\text{B}2}$). (b) $\text{MoNb}_{\text{B}2}$ and MoNb constructed by VCA (MoNb_{VCA}). (c) Nb and $\text{MoZr}_{\text{B}2}$. (d) Variations of lattice parameters of four-atom tetragonal supercell in the OP under different ε_{11} for Mo, Nb, and $\text{MoNb}_{\text{B}2}$.

We then repeated the same calculations in Mo-W alloys with the B2 lattice structure. The results are listed in Fig. S1 in the Supplemental Material [28] and highlighted in Fig. 2 for typical examples. If alloying elements are from group VI, such as Cr in Fig. 2(a), the alloy's stress-strain curves behave similarly to those of pure Mo and the alloy is intrinsically brittle. As shown in Figs. 2(b) and 2(d), if the metals and alloys have fewer valence electrons, such as MoNb with an average of 5.5 valence electrons per atom, the shear instability occurs before σ_{11}^{IT} along the TP, so they are intrinsically ductile. If the metals and alloys have even fewer valence electrons, such as MoZr with the same number of average valence electrons per atom as Nb, they also have almost the same stress-strain curves and shear failure mode as those of Nb shown in Fig. 2(c).

These similarities of stress-strain curves and failure modes suggest that these brittle-ductile transitions may be dominated by band-filling effects. To explore this point, we used pseudopotentials of Mo-Nb binary alloys in the VCA scheme [22] to calculate the deformation behaviors of MoNb, as shown in Fig. 2(b). Surprisingly, although we used totally different calculation methods, B2-MoNb and VCA-MoNb behave almost identically and are both intrinsically ductile. This is strong evidence that the ideal deformation behaviors (i.e., the ideal stress versus strain relationship) of these alloys are insensitive to the local ionic character, but instead depend mostly on the global electronic structure.

Previously the variations of elastic constants under tensile strain [8,14] and resolved shear stress [11,29] were used to explain the above shear instabilities. From the perspective of the electronic structure, we can use the concept of a Jahn-Teller distortion to describe the above phenomena [18]. As shown in Figs. 1(c) and 1(d), if there are partially occupied orbitals that are degenerate because of molecular symmetry, the molecule will deform to break this symmetry and thereby split the degenerate orbitals. As a result of this splitting, the state with lower energy becomes fully occupied, and the state with higher energy remains empty, and the total electronic energy decreases.

A similar picture can describe a solid-state system: Lee and Hoffmann demonstrated that if there are large numbers of partially occupied Bloch orbitals whose \mathbf{k} are equivalent according to the symmetry of the crystal structure, then a Jahn-Teller distortion can occur [19]. They used this concept to explain the bcc-bct (body-centered tetragonal)-fcc (face-centered cubic) transition for transition metals and found that such transitions depend on the number of electrons, whose variations can shift the Fermi energy level in band structures and density of states (DOS) in order to change the population of symmetry-equivalent orbitals close to the Fermi level.

Lee and Hoffmann only investigated the lattice structures at equilibrium states. We study the alloys under tensions that can change the band structure and shift the Fermi level.

Figure 3 and Figs. S2 and S3 of the Supplemental Material [28] show the band structures of pure Mo, W, B2-MoNb, VCA-MoNb and B2-WTa in four-atom tetragonal supercells for various ε_{11} . To clarify the effects of the symmetry-equivalent Bloch orbitals, the band structures are plotted along a \mathbf{k} -space path with tetragonal symmetry [Figs. 1(a) and 3(a)]. We highlight the 12th band since it is close to the Fermi level and drives the Jahn-Teller distortion. In the tetragonal path, X_2 ($[0\frac{1}{2}0]$) and X_3 ($[00\frac{1}{2}]$) are symmetrically identical [Fig. 3(a)] so that their corresponding eigenvalues are the same [Fig. 3(b)]. As shown in Fig. 3(c), the 12th band for pure Mo has eigenenergies of ~ 1 eV below the Fermi level at X_2 and X_3 when $\varepsilon_{11} = 0.10$. As ε_{11} continues to increase, these eigenenergies shift up towards the Fermi level so that more and more symmetry-equivalent orbitals surrounding X_2 and X_3 become partially occupied. At the critical strain

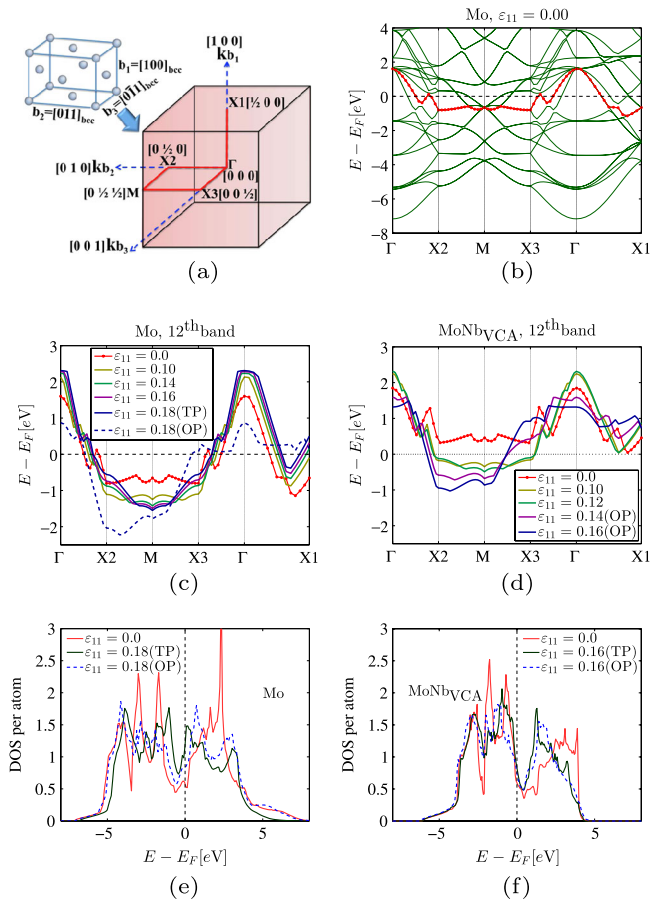


FIG. 3 (color online). (a) Symmetric \mathbf{k} points in the reciprocal space based on four-atom tetragonal supercells for band structure plots. (b) Band structures of Mo in four-atom tetragonal supercell at equilibrium. The 12th band is highlighted in red color with dots. (c),(d) The 12th band of Mo and MoNb_{VCA} four-atom tetragonal supercells under different ε_{11} , respectively. The horizontal axes from different ε_{11} are stretched to match the symmetry \mathbf{k} points when $\varepsilon_{11} = 0$. (e),(f) Density of states (DOS) for Mo and MoNb_{VCA} under different ε_{11} .

($\varepsilon_{11} = 0.18$), the Jahn-Teller distortion occurs breaking the symmetry of X_2 and X_3 . The eigenenergies of the 12th band surrounding X_2 decrease and the corresponding orbitals are fully occupied, but eigenenergies of the 12th band surrounding X_3 increase and some related orbitals are unoccupied.

As shown in Fig. 3(d) and Fig. S3 of the Supplemental Material [28], this symmetry-breaking phenomenon becomes more significant in VCA-MoNb and B2-MoNb. Both have similar band structures under increasing ε_{11} . When $\varepsilon_{11} = 0.10$, the 12th band at X_2 and X_3 of the VCA-MoNb four-atom tetragonal supercells is just ~ 0.2 eV below the Fermi level. When $\varepsilon_{11} = 0.14 \sim 0.16$, the Jahn-Teller distortion occurs. Decreasing the number of electrons shifts the Fermi level down relative to the band structure, so less strain is required to make the 12th band partially occupied surrounding X_2 and X_3 , and the shear instability occurs earlier relative to σ_{11}^{IT} along the TP. In addition, the band structures along the symmetric paths in the first Brillouin zones of one-atom primitive cells [30] are plotted in Figs. S4 and S5 of the Supplemental Material [28], where the same concentration-dependent Jahn-Teller distortion can also be observed for pure Mo and VCA MoNb. A similar trend is found for the DOS of pure Mo and VCA-MoNb in Figs. 3(e) and 3(f). For pure Mo at the equilibrium state, the Fermi level is located between two peaks so the DOS at the Fermi level is very small. Shifting the band structure by removing electrons and/or increasing ε_{11} can increase the DOS near the Fermi level, and thus increases the driving force for the Jahn-Teller distortion. After the distortion, DOS peaks just below and above the Fermi level shift further away from the Fermi level to decrease energies.

To model these band-filling effects, we can use the VCA scheme to construct pseudopotentials for Mo binary alloys with various concentrations and estimate the critical concentration for the intrinsic brittle-intrinsic ductile transition. The stress-strain curves and band structures of VCA $\text{Mo}_{1-x}\text{Nb}_x$ ($x = 0.0, 0.1, \dots, 0.5$) are plotted (details in Figs. S6 and S7 of the Supplemental Material [28]). As the Nb concentration increases, the strain corresponding to σ_{11}^{IT} increases (decreases) gradually for the TP (OP), respectively. For $\text{Mo}_{0.8}\text{Nb}_{0.2}$, its critical ε_{11} corresponding to σ_{11}^{IT} along the OP (0.16) is already smaller than its counterpart in the TP (0.18) because of the shear instability, which indicates that only an ~ 0.2 electron decrease per atom can make Mo alloys intrinsically ductile. If we further replace Nb by Ti or Zr that have two fewer valence electrons than Mo, the transition concentration could be as low as ~ 10 mol %. This composition might be stabilized through high temperature melting followed by a fast quench [31]. Our calculations suggest that these alloys may be more ductile than pure Mo.

We considered the possibility that the ideal strength, and therefore the intrinsic brittleness or intrinsic ductility, is

determined by a phonon instability [32]. We calculated the phonon dispersion relations for the $\text{Mo}_{1-x}\text{Nb}_x$ alloys under [100] tension (details in Fig. S8 of the Supplemental Material [28]). The results show that soft modes with imaginary frequencies appear only after the elastic tensile or shear failure. This confirms that the intrinsic brittle-intrinsic ductile transition is indeed determined by the transition of the elastic instability mode from tensile to shear failure. We also emphasize that the predictions are made for $T = 0$ K. In reality thermal fluctuation might also affect the dislocation nucleation events [33], and dislocation mobility and grain boundaries are other important factors that also control the ductile-brittle transition [5,34]. Nevertheless, the current agreement between experimental trends and simulation results for group V and VI metals strongly support that the intrinsic ductility determined by first-principles calculations is a good initial criterion to explain the ductility and toughness of real alloys [1,10,11,14].

In summary, the intrinsic ductility (brittleness) of bcc refractory metals is assessed by whether shear instability occurs before (after) ideal tensile stress along the symmetric tetragonal path under [100] tension. Tensile strain alters the band structures of these alloys, and changes the position of the Fermi level relative to a group of highly degenerate Bloch states. Once these states are partially filled, a solid-state Jahn-Teller distortion breaks the tetragonal symmetry, splitting the states and inducing the shear instability. Alloying additions, to the extent that they shift the Fermi level, can be used to tune the critical strain for the shear instability and the corresponding intrinsic failure mode. This concept not only yields a systematic strategy and quantitative criterion to design ductile bcc refractory alloys, but also provide a beautiful example where well-established theories in chemistry can be extended to explain phenomena in material mechanical properties.

L. Q. and D. C. C. acknowledge support by the Electric Power Research Institute. The authors also acknowledge helpful discussions with Dr. Lorenz Romaner.

*dcchrzan@berkeley.edu

- [1] S. Zinkle and N. Ghoniem, *Fusion Eng. Des.* **51–52**, 55 (2000).
- [2] M. El-Genk and J. Tournier, *J. Nucl. Mater.* **340**, 93 (2005).
- [3] J. H. Perepezko, *Science* **326**, 1068 (2009).
- [4] A. Wronski, A. Chilton, and E. Capron, *Acta Metall.* **17**, 751 (1969).
- [5] P. Gumbsch, J. Riedle, A. Hartmaier, and H. Fischmeister, *Science* **282**, 1293 (1998).
- [6] G. Liu, G. J. Zhang, F. Jiang, X. D. Ding, Y. J. Sun, J. Sun, and E. Ma, *Nat. Mater.* **12**, 344 (2013).
- [7] A. Kelly and N. H. MacMillan, *Strong Solids (Clarendon, Oxford, 1986)*.
- [8] J. Morris and C. Krenn, *Philos. Mag. A* **80**, 2827 (2000).
- [9] D. Roundy, C. R. Krenn, M. L. Cohen, and J. Morris, *Phys. Rev. Lett.* **82**, 2713 (1999).

- [10] D. Roundy, C. Krenn, M. Cohen, and J. W. Morris, *Philos. Mag. A* **81**, 1725 (2001).
- [11] W. Luo, D. Roundy, M. L. Cohen, and J. W. Morris, *Phys. Rev. B* **66**, 094110 (2002).
- [12] D. Clatterbuck, D. Chrzan, and J. Morris, *Acta Mater.* **51**, 2271 (2003).
- [13] T. Li, J. W. Morris, and D. C. Chrzan, *Phys. Rev. B* **70**, 054107 (2004).
- [14] N. Nagasako, M. Jahnatek, R. Asahi, and J. Hafner, *Phys. Rev. B* **81**, 094108 (2010).
- [15] X. Li, S. Schönecker, J. Zhao, B. Johansson, and L. Vitos, *Phys. Rev. B* **87**, 214203 (2013).
- [16] F. Milstein and S. Chantasiriwan, *Phys. Rev. B* **58**, 6006 (1998).
- [17] M. Sob, L. Wang, and V. Vitek, *Mater. Sci. Eng. A* **234**, 1075 (1997).
- [18] H. Jahn and E. Teller, *Proc. R. Soc. A* **161**, 220 (1937).
- [19] S. Lee and R. Hoffmann, *J. Am. Chem. Soc.* **124**, 4811 (2002).
- [20] G. Kresse and J. Furthmüller, *Phys. Rev. B* **54**, 11169 (1996).
- [21] P. Giannozzi, S. Baroni, N. Bonini, M. Calandra, R. Car, C. Cavazzoni, D. Ceresoli, G. L. Chiarotti, M. Cococcioni, I. Dabo, *et al.*, *J. Phys. Condens. Matter* **21**, 395502 (2009).
- [22] L. Romaner, C. Ambrosch-Draxl, and R. Pippin, *Phys. Rev. Lett.* **104**, 195503 (2010).
- [23] G. Kresse and D. Joubert, *Phys. Rev. B* **59**, 1758 (1999).
- [24] J. P. Perdew, J. A. Chevary, S. H. Vosko, K. A. Jackson, M. R. Pederson, D. J. Singh, and C. Fiolhais, *Phys. Rev. B* **46**, 6671 (1992).
- [25] N. Troullier and J. L. Martins, *Phys. Rev. B* **43**, 1993 (1991).
- [26] J. P. Perdew, K. Burke, and M. Ernzerhof, *Phys. Rev. Lett.* **77**, 3865 (1996).
- [27] M. Fuchs and M. Scheffler, *Comput. Phys. Commun.* **119**, 67 (1999).
- [28] See Supplemental Material at <http://link.aps.org/supplemental/10.1103/PhysRevLett.112.115503> for stress-strain curves, band structures and phonon dispersion curves of alloys at different strain states.
- [29] T. Li, J. W. Morris, and D. C. Chrzan, *Phys. Rev. B* **73**, 024105 (2006).
- [30] W. Setyawan and S. Curtarolo, *Comput. Mater. Sci.* **49**, 299 (2010).
- [31] L. Kecskes, *Materials and Manufacturing Processes* **14**, 123 (1999).
- [32] D. M. Clatterbuck, C. R. Krenn, M. L. Cohen, and J. W. Morris, *Phys. Rev. Lett.* **91**, 135501 (2003).
- [33] M. Khantha, D. P. Pope, and V. Vitek, *Phys. Rev. Lett.* **73**, 684 (1994).
- [34] L. Lim and T. Watanabe, *Acta Metall. Mater.* **38**, 2507 (1990).